J. Eng. Technol. Sci., Vol. 53, No. 5, 2021, 210504

Characteristics of Rainfall-Induced Slope Instability in Cisokan Region, Indonesia

Sugeng Krisnanto[1*], Harianto Rahardjo[2], Rendy Dwi Kartiko[3], Alfrendo Satyanaga[4], Joko Nugroho[5], Netto Mulyanto[6], Pudjo Santoso[6], Achmad Hendiarto[6], Didit Beny Pamuji[7] & Saraswati Noor Rachma[7]

[1]Geotechnical Engineering Research Group, Faculty of Civil and Environmental Engineering, Bandung Institute of Technology, CIBE Building Level 5, Room CIBE 0506, Jalan Ganesa No. 10, Bandung 40132, Indonesia
[2]School of Civil & Environmental Engineering, Nanyang Technological University, Blk. N1, #1B-36, 50 Nanyang Avenue, Singapore 639798, Singapore
[3]Applied Geology Research Group, Faculty of Earth Sciences and Technology, Bandung Institute of Technology, Jalan Ganesa No. 10, Bandung 40132, Indonesia
[4]Department of Civil and Environmental Engineering, Nazarbayev University, 53 Kabanbay Batyr Ave, 010000, Nur-Sultan, Kazakhstan
[5]Water Resources Engineering Research Group, Faculty of Civil and Environmental Engineering, Bandung Institute of Technology, CIBE Building Level 5, Room CIBE 0531, Jalan Ganesa No. 10, Bandung 40132, Indonesia
[6]Prima Layanan Nasional Enjiniring, Jakarta 12310, Indonesia
[7]Civil Engineering Program, Faculty of Civil and Environmental Engineering, Bandung Institute of Technology, Jalan Ganesa No. 10, Bandung 40132, Indonesia
*E-mail: sugeng.krisnanto@ftsl.itb.ac.id

Highlights:

- Analyses of rainfall-induced slope instability by considering saturated and unsaturated soil mechanics.
- The use of two independent stress-state variables for unsaturated soil mechanics.
- Field observation of an event of rainfall-induced slope instability.
- Numerical analyses incorporating flux boundary conditions.
- Saturated-unsaturated soil mechanics analysis using the extended shear strength method and the total cohesion method.

Abstract. A 25.5 km long access road has been constructed in a hilly area in Cisokan region. Several slope instabilities occurred during the rainy season, particularly at the end of heavy rainfall. A comprehensive study was performed to understand the characteristics of rainfall-induced slope instability. The study consisted of field observation, analyses of field and laboratory test data, and numerical analyses. The study revealed that in general there were two categories of slopes with instability characteristics: (i) slopes with a significant groundwater level increase during rainfall; (ii) slopes with an insignificant groundwater level increase during rainfall. In the first category, the slope instability was caused by a loss of matric suction and eventually the pore-water pressure, u_w became positive

Received November 5th, 2020, 1st Revision January 8th, 2021, 2nd Revision February 23rd, 2021 Accepted for publication March 31st, 2021.
 ISSN: 2337-5779, DOI: 10.5614/j.eng.technol.sci.2021.53.5.4

as indicated by an increase of the groundwater level. In the second category, the slope instability was caused by a loss of matric suction without a rise in pore-water pressure, u_w, to a positive magnitude. Two empirical curves of slope stability were developed as a preliminary guidance to assess slope stability during rainfall in the region.

Keywords: *empirical slope stability curve; field observation; numerical analysis; rainfall-induced slope instability; unsaturated soil.*

1 Introduction

A 25.5 km long access road has been constructed in Cisokan region, West Java Province, Indonesia (Figure 1). Most parts of the access road are situated in hilly areas, which consists of two lanes-two ways undivided. The road was constructed by a combination of cutting the hillside for one lane and filling the valley side for the other. The road is located in the Citarum and Rajamandala formations [1]. It passes the unit of tuffaceous breccia, lava, sandstone, conglomerate (Pb), tuffaceous lake deposits (Q1), pumice tuff, tuffaceous sandstone (Mt), breccia and the sandstone member of the Citarum formation (Mtb), the sandstone-siltstone member of the Citarum formation (Mts), and the clay, marl, and quartz sandstone member of the Rajamandala formation (Omc).

Several slope instabilities occurred in the rainy season during the construction works. Slope instabilities particularly occurred after several days of antecedent rainfall. Rainfall-induced slope instability has occurred several times in the Cisokan region [2-9] as well as in other regions in Indonesia [10,11]. Global warming, exacerbated by human activities, has led to changing weather patterns such as higher rates of precipitation [12]. Rainfall infiltration has been identified as one of the main triggering factors of slope instability in tropical regions [13-16]. Rainfall infiltration causes the reduction of matric suction and reduces the shear strength of the soil. The reduction of the shear strength lowers the resisting force against slope instability and lowers the factor of safety, *FS*, against slope instability [13,14]. As unprecedented rainfall intensities are expected in the future, it is important to investigate the effect of rainfall on the stability of unsaturated soil slopes, especially in tropical countries like Indonesia.

Slope stability analysis utilizing saturated-unsaturated shear strength has been implemented in several countries in Asia [12,17,18]. Some new advancements of the method have been achieved, such as the use of an analytical formulation to predict the change in the factor of safety for a slope subjected to infiltration [19] and the use of discrete element modeling for predicting run-out characteristics of rainfall-induced landslides [18]. Despite this advancement, slope stability analysis utilizing saturated-unsaturated shear strength is not yet implemented as

a standard practice of rainfall-induced slope stability analysis in Indonesia. Laboratory tests and field measurements dedicated to this analysis are practically unavailable. This creates difficulties in quantifying the characteristics of rainfall-induced slope instability in the region.

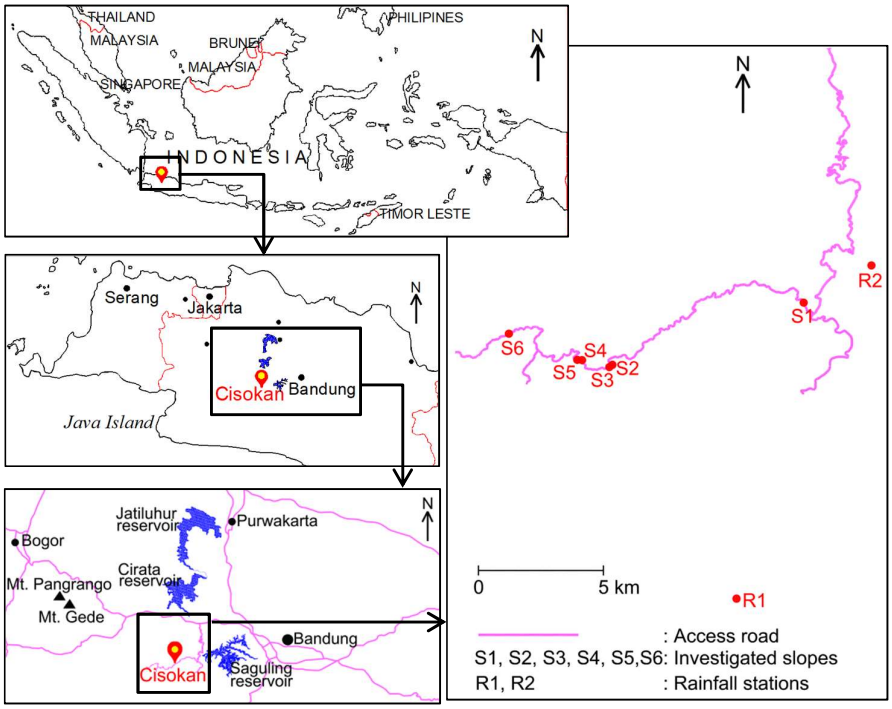

Figure 1 Location of the investigated slopes at the constructed access road at Cisokan region.

Therefore, slope stability analysis that incorporates a saturated-unsaturated soil system is urgently needed. Due to the lack of understanding of saturated-unsaturated soil mechanics and the limited availability of relevant data, the use of estimated unsaturated soil properties for analyses incorporating saturated-unsaturated soils is a reasonable step toward the application of unsaturated soil mechanics to the characterization of rainfall-induced slope instability.

This paper presents a study to understand the characteristics of rainfall-induced slope instability in the Cisokan region, West Java Province, Indonesia. The study combined field observation, analyses of field and laboratory testing data, and numerical analyses. The theory of unsaturated soil mechanics was implemented despite the limited data available in most geotechnical engineering practices in

Indonesia.

2 Methodology

The study started with field observations, followed by the collection and analyses of antecedent rainfall and soil property data. Considering the field conditions, soil properties and rainfall data, numerical analyses were performed to understand the rainfall-induced slope instability characteristics of six slopes in the region. The extended shear strength [20,21] and the total cohesion methods [21] were utilized in the numerical analyses. In the extended shear strength method, two independent stress state variables are required to describe the behavior of unsaturated soil [20-22]: net normal stress, σ-u_a, and matric suction, u_a-u_w, where σ is the total normal stress, u_a is the pore-air pressure and u_w is the pore-water pressure. The extended shear strength, τ_{ff} is defined as [21]:

$$\tau_{ff} = c' + (u_a - u_w)_f \tan \phi^b + (\sigma - u_a)_f \tan \phi' \quad (1)$$

where c' is the effective cohesion, $(\sigma\text{-}u_a)_f$ is the net normal stress state on the failure plane at failure, ϕ' is the angle of internal friction associated with the net normal stress state variable, $(u_a\text{-}u_w)_f$ is the matric suction on the failure plane at failure, and ϕ^b is the angle indicating the rate of increase in shear strength relative to the matric suction. To obtain the value of the matric suction, a seepage analysis was performed. In this paper, the soil-water characteristic curve (SWCC) for the seepage analysis was predicted utilizing the index properties data with the equations proposed by Perera, *et al.* [23], which predicts Fredlund & Xing's [24] SWCC fitting parameters (a, n, m and $(u_a\text{-}u_w)_r$):

$$a = 32.835 \ln(wPI) + 32.438 \quad (2)$$

$$n = 1.421(w\text{PI})^{-0.3185} \quad (3)$$

$$m = -0.2154 \ln(wPI) + 0.7145 \quad (4)$$

$$(u_a - u_w)_r = 500 \quad (5)$$

where wPI is the weighed plasticity index, which is equal to the product of P_{200} (expressed as a decimal) and the plasticity index (PI). P_{200} is the percentage passing through a Nr. 200 sieve. In this paper, the permeability function was calculated indirectly using the method of Fredlund & Rahardjo [21] by utilizing SWCC and the saturated permeability, k_s, as follows:

$$k_w(\theta_w)_i = \frac{k_s}{k_{sc}} A_d \sum_{j=1}^{m} \{(2j + 1 - 2i)(u_a - u_w)_j^{-2}\} \quad (6)$$
$$i = 1, 2, \ldots, m$$

where $k_w(\theta_w)_i$ is the predicted water coefficient of permeability for a volumetric

water content; θ_w corresponds to the i-th interval; i is the interval number, which increases as the volumetric water content decreases; m is the total number of the intervals between the saturated volumetric water content, θ_s and the lowest volumetric water content on the experimental soil-water characteristic curve, θ_L, j is a counter from i to m; k_s is the measured saturated coefficient of permeability; k_{sc} is the computed saturated coefficient of permeability, A_d is the adjusting constant, and $(u_a\text{-}u_w)_j$ is the matric suction.

In the total cohesion method, the stability analysis was carried out by incorporating matric suction into the cohesion of the soil. Equation (1) is written as:

$$\tau_{ff} = c + (\sigma - u_a)_f \tan \phi' \tag{7}$$

where c is the total cohesion, which can be calculated as follows [21]:

$$c = c' + (u_a - u_w)_f \tan \phi^b \tag{8}$$

In this method, the matric suction is considered as a percentage of the matric suction in hydrostatics condition [21]. Several matric suction profiles with depth were considered in the analyses.

Field observation of slope instability was performed in the investigated area. The instability condition of each investigated slope was used to calibrate the analysis results equivalent to the condition where the factor of safety of the slope was equal to 1. Rainfall data was collected and antecedent rainfall corresponding to the slope instability was used in the analysis. Rainfall intensities at slope locations were interpolated from rainfall data recorded at adjacent rainfall stations. Index soil properties were obtained from the results of laboratory tests carried out for this construction [25]. The extended Mohr-Coulomb shear strength properties were estimated from the index properties of the soils. The Seep/W software [26] was used in the saturated-unsaturated transient seepage analysis. The computed pore-water pressure from Seep/W was then used in the slope stability analysis with the simplified Bishop's method [27]. The slope stability analysis was performed utilizing Slope/W [28].

Slope stability analyses were performed for the slopes presented in Table 1. The analyses were performed using the extended shear strength method for slopes no. 2 and 6. Slope no. 2 (21.7° slope angle) represents a slope that is less steep than the standard slope gradient 2H:1V to 1.5H:1V or 26.6° to 33.7° slope angle [29,30]. Slope no. 6 (52.1° slope angle) represents a slope that is steeper than the standard slope gradient that can be found at some hilly regions in Indonesia [e.g. 10,11]. In addition, the slope stability analyses using the total cohesion method were performed for all six slopes listed in Table 1.

Table 1 Details of the slopes experiencing instability in March 2019.

Slope No.	Slope Condition						Slope Unstable Part			
	Type	Height (m)	Angle (deg)	Gradient (H:V)	Hard Layer Depth (m)	Low Groundwater Depth (m)	Classification	Thickness (m)	Soil Type (USCS)	Average N-SPT
1	Fill	7.2	23.0	2.4:1	11.6	5.9 (9 Apr 2019)	Rotational	3.3	Elastic Silt with Sand (MH)	2
2	Fill	12.6	21.7	2.5:1	7.3	3.8 (28 Apr 2019)	Rotational	3.3	Elastic Silt with Sand (MH)	4
3	Fill	11.7	23.0	2.4:1	13.2	5.9 (22 Mar 2019)	Rotational	3.1	Elastic Silt with Sand (MH)	5
4	Fill	9.4	31.3	1.6:1	8.1	5.0 (30 Mar 2019)	Rotational	2.1	Elastic Silt with Sand (MH)	
5	Fill	10.4	24.4	2.2:1	7.4	5.5 (5 Apr 2019)	Rotational	2.9	Sandy Silt (ML)	
6	Fill	35.0	52.1	0.8:1	8.4	8.4 (3 Jun 2019)	Rotational	2.0	Elastic Silt with Sand (MH)	8

3 Field Observation

Details of the slopes experiencing instability in March 2019 are presented in Table 1. The locations of the slopes are shown in Figure 1. The thickness of the unstable part of the slope was measured at the mid cross-section. The groundwater level was observed on non-rainy days and is called the 'low groundwater level' in this paper. Table 1 shows that all the observed slope instabilities occurred above the groundwater level, indicating the failure occurred within the unsaturated zone of the soil. Table 1 also shows that the thickness of the unstable part of the slopes was less than the depth of the hard layer, indicating that the slip surfaces were developed without the resistance from the hard layer. The field conditions of slopes no. 2 and 6 in unstable condition are shown in Figures 2 and 3.

(a)

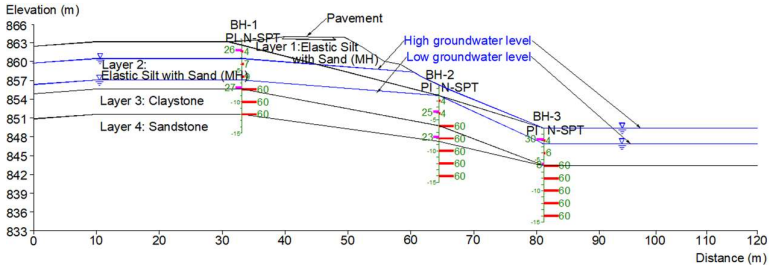

(b)

Figure 2 Field condition of slope at location no. 2: (a) photo, (b) cross section.

(a)

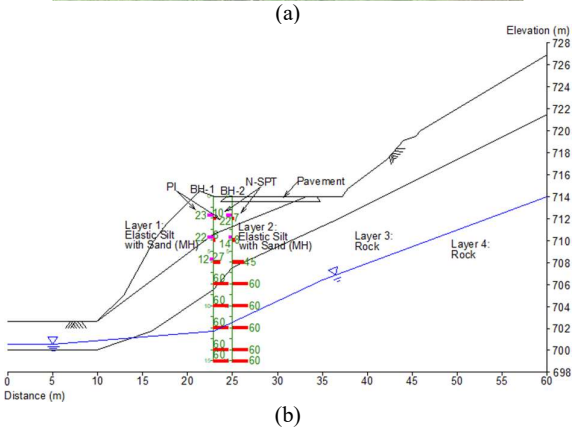

(b)

Figure 3 Field condition of slope at slope no. 6: (a) photo, (b) cross section.

4 Rainfall and Soil Properties

4.1 Rainfall

The daily rainfall data from 1 February to 31 March 2019 from two adjacent rainfall stations, R1 and R2 (Figure 1), are shown in Figure 4(a). The distance of slopes nos. 2 to 6 to both rainfall stations is about 11 km and the distances of slope no. 1 to rainfall stations R1 and R2 are 12 km and 3 km, respectively. Slope instability occurred on 8 March 2019 and Figure 4(a) shows that from 4 to 6 February 2019 was a period with minimum daily rainfall. It was assumed that the increase of pore-water pressure, u_w, caused by the rainfall before 4 February 2019 dissipated in the period between 4 and 6 February 2019. Therefore, the rainfall between 7 February and 8 March 2019 was considered as the antecedent rainfall that caused the slope instability on 8 March 2019. Figure 4(a) also indicates that slope instability did not occur after the high daily rainfall alone (on 9 and 13 February and 2 March 2019) but after several days of antecedent rainfall.

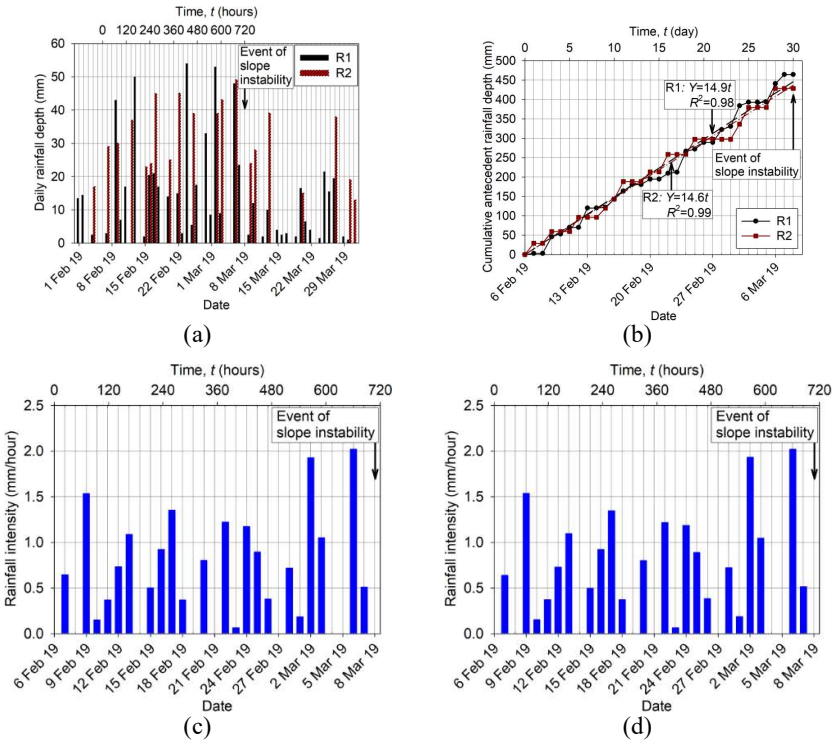

Figure 4 (a) Daily rainfall depth vs. time data, (b) cumulative antecedent rainfall depth, (c) interpolated rainfall intensity vs. time for slope no. 2, (d) interpolated rainfall intensity vs. time for slope no. 6.

It seemed that two high rainfall events (on 2 and 6 March 2019) contributed significantly to further reduce the stability of the slopes. These high rainfall events were recorded in both rainfall stations R1 and R2 (Figure 4(a)).

The plot of cumulative rainfall depth between 8 February and 8 March 2019 (Figure 4(b)) indicates that the rainfall depths were close between R1 and R2 data. In addition, it also indicated that a rate of increase in cumulative rainfall depth of 15 mm per day in 4 consecutive weeks may cause rainfall-induced slope instability in this region (Figure 4(b)). For the slope stability analysis using the extended shear strength method, the daily rainfall depth for slopes no. 2 and 6 were interpolated using the inverse distance weighting method [31]. The rainfall intensity was computed from the daily rainfall depth data calculated by assuming a uniform distribution of daily rainfall in 24 hours (Figures 4(c) and 4(d)).

4.2 Soil Properties

A summary of the soil index properties is shown in Figure 5. The saturated unit weight varies from 16 kN/m^3 to 18 kN/m^3 (Figure 5(a)). The variation of plasticity index, PI is presented in Figure 5(b) with average values of 29.2%, 23.0%, 20.8%, 24.9%, 12.9%, 18.6% for slopes no. 1 to 6, respectively. The variation of PI vs. N-SPT [32] is shown in Figure 5(c). There is a decreasing trend of PI as the N-SPT value increases. The plasticity index can be related to the effective friction angle, ϕ' [33,34], and the undrained shear strength, s_u [33-36]. The N value of the standard penetration test (N-SPT) can be related to the undrained shear strength, s_u [33,36]. Standard penetration test, SPT is performed in most geotechnical engineering projects in Indonesia [37,38]. Hence, it is important to have an indirect correlation between N-SPT and PI since both are performed more often than the triaxial test to obtain undrained and drained shear strength parameters.

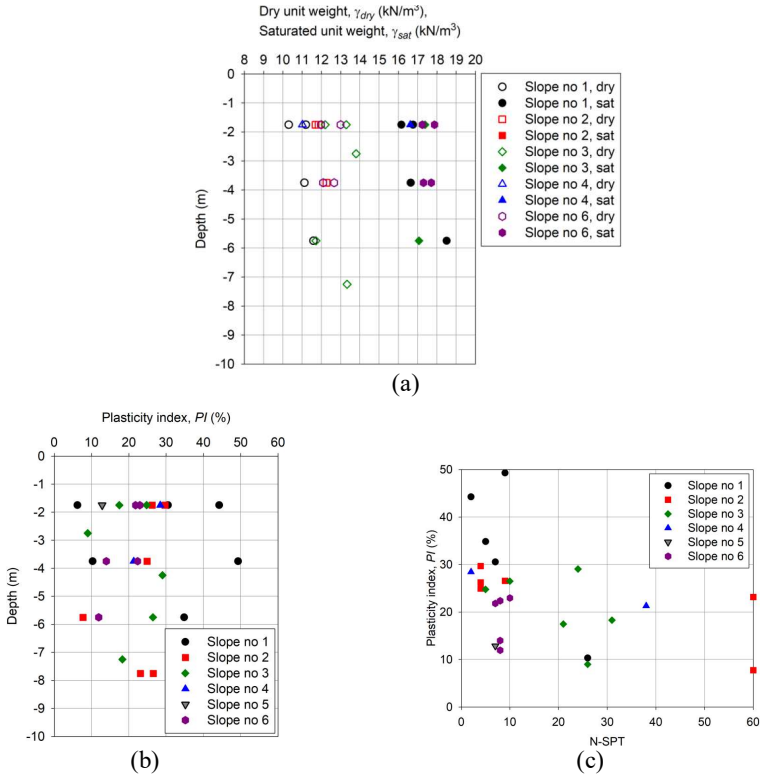

Figure 5 Soil properties obtained in June 2019: (a) variation of unit weight, γ with depth, (b) variation of plasticity index (PI) with depth, (c) PI vs. N-SPT (Data from [25]).

5 Numerical Analysis

In the analyses, the effective friction angle, ϕ', was taken from the curve of the relationship between ϕ' and PI [33,34]. For silt layers, the average to maximum PI from each location (Figure 5(b)) was used to obtain ϕ' from this relationship. In each location, a value of the effective cohesion, *c'*, between 0 and 15 kPa was used. This is the range of the effective cohesion for silt layers in the region [39]. The value of ϕ^b was estimated as 0.25 times ϕ'. The values of *c'* and ϕ^b were in the range of several measured data for cohesive soils [21]. For claystone layers, the effective cohesion and the effective friction angle parameters from a project in this region were used [39]. The recommended parameters were obtained from a combination of values from laboratory tests and field geological observations. A value of ϕ^b equal to zero was used in the project, since the unsaturated shear strength characteristics of claystone in the region is not understood. A value of ϕ^b equal to zero gave the lowest value of the unsaturated shear strength for claystone.

The saturated permeability, k_s, was predicted as the value of saturated permeability calculated from the results of the consolidation test multiplied by a factor greater than one to accommodate the sample size effect [40,41]. A hydrostatics condition using a low groundwater level for each slope in Table 1 was used as the initial condition. In the analysis, the maximum matric suction was limited to 100 kPa. Head boundary conditions were applied on the left and right boundaries of the numerical models, corresponding to the position of the groundwater level at each boundary. Rainfall intensity between 6 February and 8 March 2019 (Figures 4(c) and 4(d)) was used as the flux boundary condition on the ground surface in the numerical models. The flux boundary condition was applied to the ground surface except in areas covered by road pavement.

5.1 Slope No. 2

Slope no. 2 is located within the unit of the sandstone-siltstone member of Citarum formation (Mts). The unit consists of well-bedded sandstone intercalated with siltstone, claystone, greywacke, and breccia [1]. The soil properties used in the analysis of slope no. 2 are shown in Table 2.

Table 2 Soil properties used in the analysis of slope no. 2.

Parameters	Layers 1 and 2	Layer 3	Layer 4
Material type	Elastic silt with sand (MH)	Claystone	Sandstone
Saturated permeability, k_s (m/s)	1.00×10^{-8}	Impermeable	Impermeable
Unit weight, γ (kN/m^3)	17.5	22	22
Effective cohesion, c' (kPa)	6.5	25	25
Effective friction angle, ϕ' (deg)	27.5	16	16
ϕ^b (deg)	6.8	0	0

Layers 1 and 2 of slope no. 2 (Figure 1(b)) are fill layers compacted in two different stages. The layers were compacted at the same compaction effort. Therefore, the same shear strength and hydraulic parameters were used for these layers (Table 2 and Figure 6).

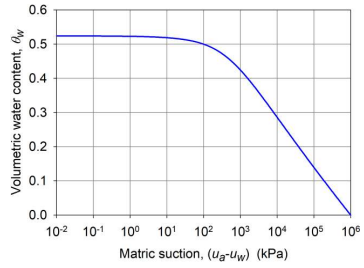

(a)

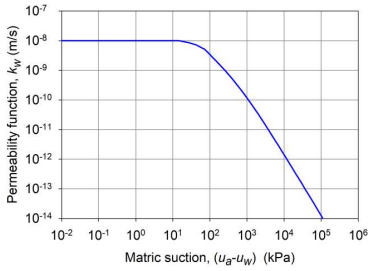

(b)

Figure 6 SWCC and permeability function of layers 1and 2 for slope no. 2: (a) SWCC, (b) permeability function.

Analysis using extended shear strength method

The SWCC and permeability function of layers 1 and 2 for slope no. 2 are shown in Figure 6. The variation of pore-water pressure versus depth at the mid part of slope no. 2 and the variation of the factor of safety versus time as obtained from the numerical analysis are shown in Figure 7. The critical failure surface and factor of safety for two selected times are shown in Figure 8. The analysis results revealed that there was an increase of the groundwater level (Figure 7) that caused the slope to lose its matric suction; eventually the pore-water pressure became positive, leading to slope instability.

In other words, the factor of safety of the slope decreases during rainfall (Figure 8). The date of slope instability event agrees with the actual date of slope failure. This shows that the analyses are in good agreement with the field data.

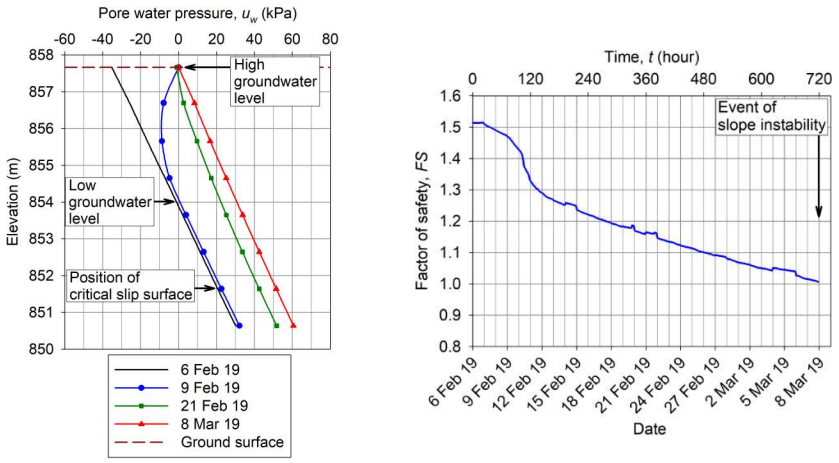

(a) (b)

Figure 7 (a) Variation of pore-water pressure u_w vs. depth at the mid-part of slope no. 2, (b) variation of factor of safety, FS vs. time, t.

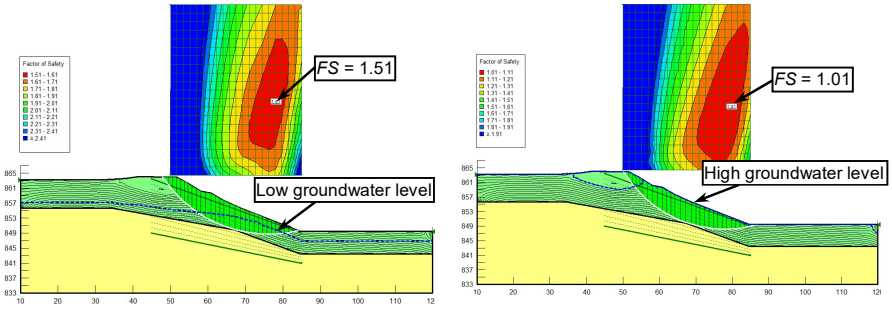

(a) (b)

Figure 8 Critical failure surface and factor of safety of slope no. 2: (a) at elapsed time 0 hours (6 February 2019), (b) at elapsed time 720 hours (8 March 2019).

Analysis using total cohesion method

As the analysis using the extended shear strength method revealed that there was an increase in the groundwater level during the event of slope instability, the analysis using the total cohesion method was performed under two conditions, namely, low groundwater level (Table 1) and high groundwater level. High groundwater level was obtained by raising the low groundwater level in the model until instability condition (i.e. FS equal to 1) was obtained. An increase of groundwater level of 3.8 m was found to cause instability. This increase of ground water level agrees with that obtained from the extended shear strength method

(Figure 7(a)). The analysis results using the total cohesion method on slope no. 2 are shown in Figure 9.

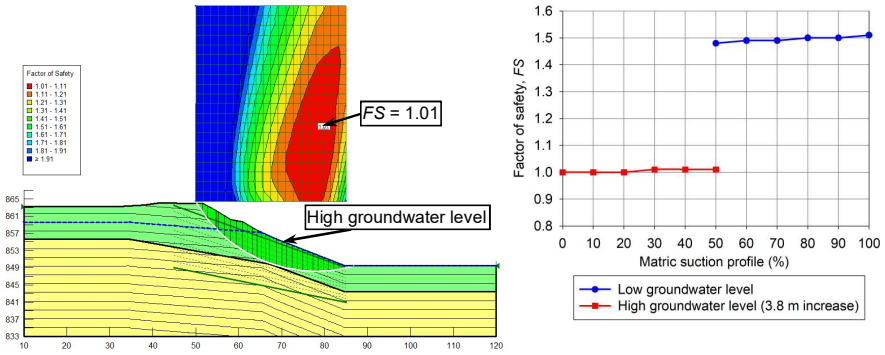

(a) (b)

Figure 9 Numerical slope stability analysis using the total cohesion method on slope no. 2: (a) result of analysis for observed failure condition (matric suction profile 0% of hydrostatics condition of high groundwater level), (b) variation of factor of safety, *FS* vs. matric suction profile and different groundwater levels.

5.2 Slope No. 6

Slope no. 6 is situated on the border between the unit of the sandstone-siltstone member of Citarum formation (Mts) and the unit of the marl, and quartz sandstone member of Rajamandala formation (Omc) [1]. The unit of Mts consists of well-bedded sandstone intercalated with siltstone, claystone, greywacke, and breccia. The unit of Omc consists of dark to black, marly clay, globigerina marl, quartz sandstone, and quartz pebbly conglomerate. The soil properties used in the analysis of slope no. 6 are shown in Table 3.

Table 3 Soil properties used in the analysis of slope no. 6.

Parameters	Layer 1	Layer 2	Layer 3	Layer 4
Material type	Elastic silt with sand (MH)	Elastic silt with sand (MH)	Rock	Rock
Saturated permeability, k_{sat} (m/s)	1.21×10^{-8}	5.24×10^{-9}	7.50×10^{-3}	Impermeable
Unit weight, γ (kN/m^3)	17	17	22	22
Effective cohesion, c' (kPa)	6.5	13	25	25
Effective friction angle, ϕ' (deg)	30.1	30.1	16	16
ϕ^b (deg)	7.5	7.5	0	0

Analysis using extended shear strength method

The SWCC and permeability function for layers 1 and 2 for slope no. 6 are shown in Figure 10. The variation of pore-water pressure, u_w versus depth in the mid-

section of slope no. 6 and the variation of factor of safety versus time as obtained from the numerical analysis are shown in Figure 11. The critical failure surface and factor of safety for two selected times are shown in Figure 12.

The analysis results show the loss of matric suction (Figure 11(a)), which reduces the factor of safety of the slope during rainfall (Figure 11(b)). The increase in the groundwater level is insignificant (Figure 12) and the date of slope instability event agrees with the actual date of slope failure in slope no 2.

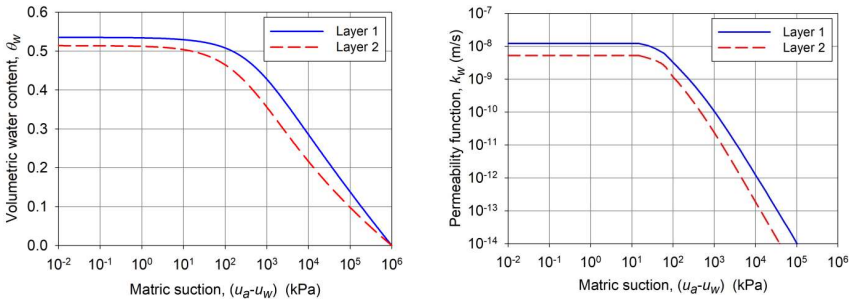

(a) (b)

Figure 10 SWCC and permeability function of layers 1 and 2 for slope no. 6: (a) SWCC, (b) permeability function.

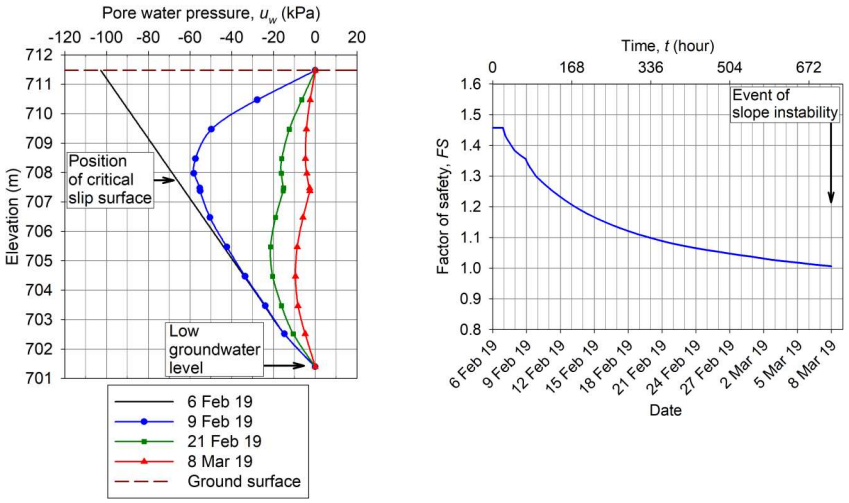

(a) (b)

Figure 11 (a) Variation of pore-water pressure, u_w vs. depth in the mid-part of slope no. 6, (b) variation of factor of safety, FS vs. time, t.

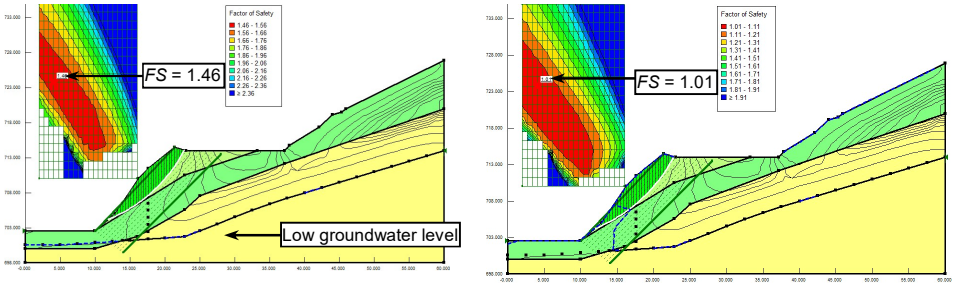

(a) (b)

Figure 12 Critical failure surface and factor of safety, *FS*, of slope no. 6: (a) at elapsed time 0 hours (6 February 2019), (b) at elapsed time 720 hours (8 March 2019).

Analysis using total cohesion method

The analysis results using the total cohesion method for slope no. 6 are shown in Figure 13. The results show that even without an increase in groundwater level, the slope became unstable (i.e. *FS* equal to 1) due to the loss of matric suction.

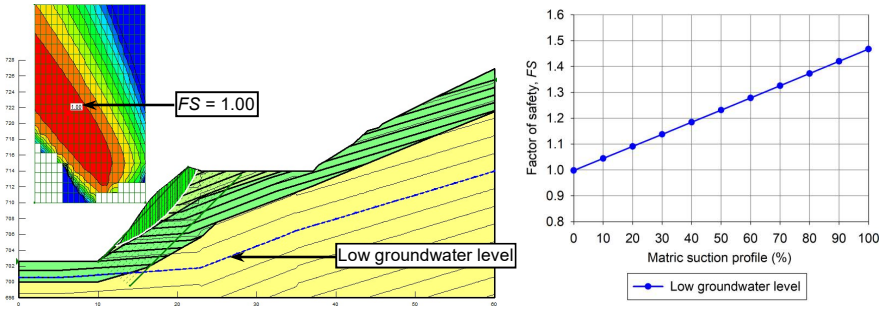

(a) (b)

Figure 13 Numerical slope stability analysis using the total cohesion method on slope no. 6: (a) result of analysis for observed failure condition (matric suction profile 0% of hydrostatic condition); (b) variation of factor of safety, *FS* vs. matric suction profile.

5.3 Other Slopes

In general, slope no. 1 is located within a unit of tuffaceous breccia, lava, sandstone, conglomerate (Pb). The unit consists of andesitic and basaltic breccia, lava, tuffaceous sandstone, and conglomerate [1]. Slopes no. 3, 4, and 5 are located within the unit of sandstone-siltstone (Mts). The unit consists of well

bedded sandstone intercalated with siltstone, claystone, greywacke, and breccia [1].

Slopes no. 1, 3, 4, and 5 were analyzed using the total cohesion method. Field observation indicated that there was a rise of the groundwater level in these locations during rain. This condition was modeled in the analysis. The results using the total cohesion method for slopes no. 1, 3, 4, and 5 are shown in Figure 14. The results indicated that the increase in groundwater level caused slope instability. In addition, the results revealed that during dry conditions, the slopes had a high factor of safety.

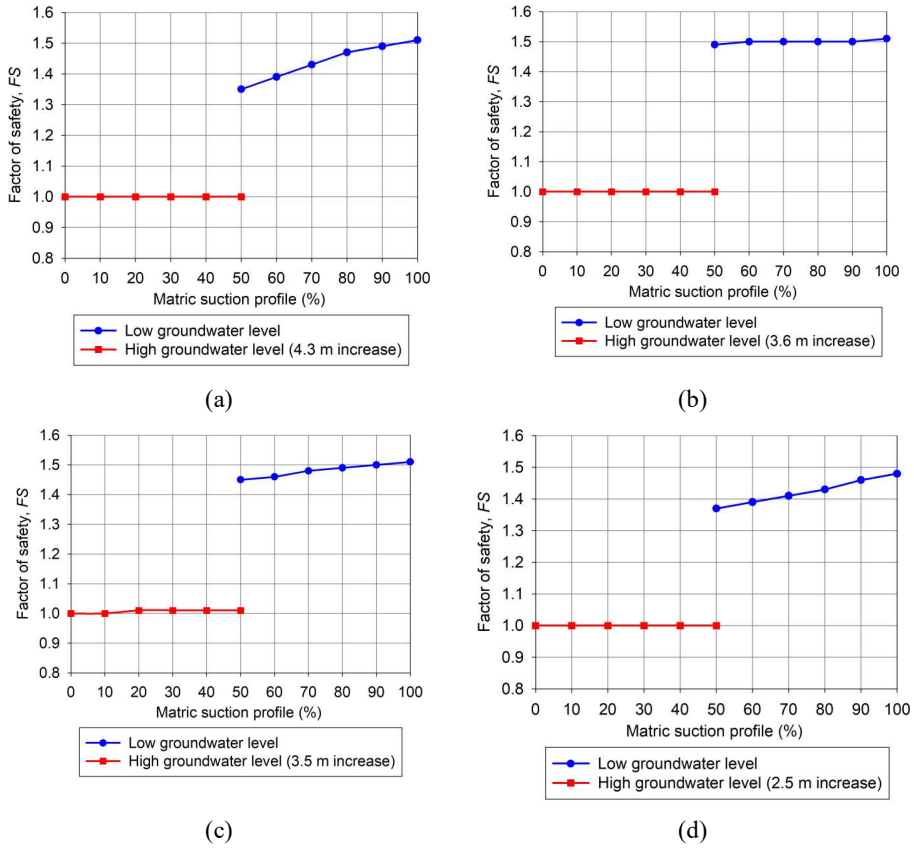

Figure 14 Variation of factor of safety, *FS* vs. matric suction profiles: (a) slope no. 1, (b) slope no. 3, (c) slope no. 4, (d) slope no. 5.

6 Discussion

From the above analyses, the slopes with of rainfall-induced slope instability characteristics in this region could be divided into two categories: (i) slopes with groundwater level increase during rainfall; (ii) slope with an insignificant groundwater level increase during rainfall. In the first category, the slope instability was caused by a loss of matric suction and eventually the pore-water pressure became positive, resulting in an increase in the groundwater level. In the second category, the slope instability was caused by the loss of matric suction without the rise of pore-water pressure to a positive value. Unstable parts were found in the layers that had similar effective shear strength values (Figures 2(b), 3(c), 8, 9, 12, and 13; Tables 2 and 3). This indicates that the groundwater increase governed the reduction of shear strength. Slopes nos. 1 to 5 fall into the first category. These slopes have an inclination angle equal to or less than 31.3°. Slope no. 6 falls into the second category. This slope has an inclination angle equal to 52.1°. By comparing slopes no. 1 and 3 it seems that the slope height did not contribute significantly to rainfall-induced slope instability. The results also indicate that for the first category of slopes, the factor of safety during dry conditions was high (±1.5). However, at high groundwater level, an increase in matric suction profile did not contribute to a significant increase of the factor of safety. This indicates that efforts to keep the groundwater level low and to maintain matric suction above the groundwater level are necessary since they contribute significantly to maintaining a high factor of safety. Further investigation is needed to understand the characteristics of rainfall-induced slope stability of slopes with an inclination angle between 31.3° to 52.1°.

A summary of the matric suction condition at slope instability is presented in Table 4. Using the field observation and test data (Table 1) and the calculated groundwater level at the event of slope stability (Table 4), two empirical curves of slope stability were developed (Figure 15). The slope instability is related to SPT since this test is used in most projects in Indonesia and the database of SPT tests in Indonesia is much larger than that of triaxial and index properties tests [37,38]. The relationship in Figure 15 serves as a preliminary guidance to assess slope stability during rainfall in the region. The regression along the X-axis covers only the values of N-SPT from 2 to 8 which correspond to soft to medium clay [33]. More observation data are required to extend the coverage of the curves. Figure 15 indicates that as the ground water depth increases, the slope stability increases, as indicated by an increase of the stable slope angle (Figure 15(a)) and a decrease of the thickness of the unstable part of the slope (Figure 15(b)). The ground water depth represents the matric suction, which plays a significant role in maintaining the stability of the slope. Figure 15 also indicates an increase of slope stability as the average N-SPT of the unstable zone of the slope increases. There is a decrease of the plasticity index as the N-SPT value

increases, as shown in Figure 5(c). Since there is an increase of the saturated friction angle with a decrease in the plasticity index [33,34], there is an increase of the saturated friction angle with an increase of the N-SPT. An increase of the saturated friction angle increases the slope stability.

The analyses presented in this paper were performed using an unstable condition (*FS* equal to 1) as a calibration factor. The precise value of the factor of safety with variation of matric suction needs to be further investigated. This highlights the need for unsaturated shear strength and unsaturated hydraulic properties measurement and for rainfall measurement with time for the analysis of rainfall-induced slope instability. In addition, monitoring of pore-water pressure is also required to verify the calculated factor of safety.

Table 4 Summary of matric suction condition at slope instability.

Slope no.	Slope height (m)	Slope angle (deg)	Slope gradient (H:V)	Back-calculation at slope instability	
				Predicted increase of groundwater level (m)	Predicted matric suction profile (% of hydrostatic)
1	7.2	23.0	2.4H:1V	4.3	0
2	12.6	21.7	2.5H:1V	3.8	0
3	11.7	23.0	2.4H:1V	3.6	0
4	9.4	31.3	1.6H:1V	3.5	0
5	10.4	24.4	2.2H:1V	2.5	0
6	35.0	52.1	0.8H:1V	0	0

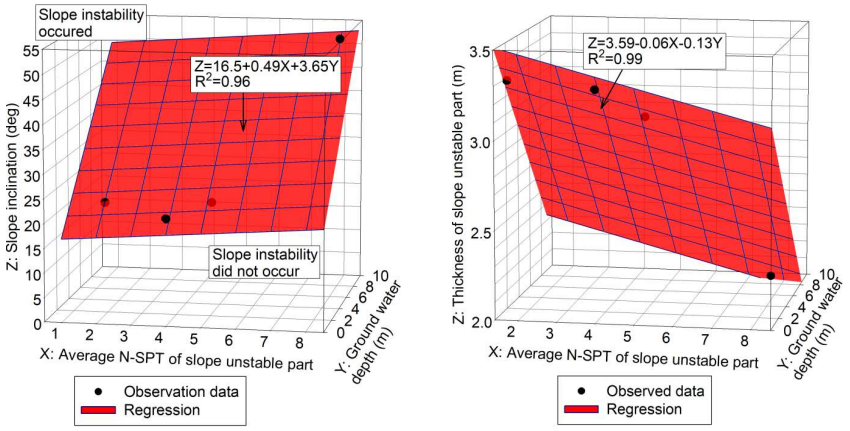

Figure 15 Empirical curve of slope stability: (a) relationship between the slope angle, the average N-SPT of the slope failure part, and the ground water depth; (b) relationship between the thickness of the slope failure part, the average N-SPT of the slope failure part, and the groundwater depth.

7 Conclusions

The application of the unsaturated soil mechanics principle played an important role in obtaining realistic results from the rainfall-induced slope stability analyses in the studied region. A rate of increase in cumulative rainfall height of 15 mm per day in 4 consecutive weeks may cause rainfall-induced slope instability in this region.

The slopes with of rainfall-induced slope instability characteristics in this region can be divided into two categories: (i) slopes with a significant groundwater level increase during rainfall (associated with slope angles equal to or less than 31.3°); (ii) slopes with an insignificant water level increase during rainfall (associated with a slope angle of 52.1°). It seems that the slope height does not contribute significantly to rainfall-induced slope instability. Two empirical curves of slope stability were developed as a preliminary guidance to assess slope stability in the region during rainfall. The relationship covers N-SPT values from 2 to 8.

The analyses also highlight the need for unsaturated shear strength and unsaturated hydraulic properties measurement, the need for rainfall measurement with time for the analysis of rainfall-induced slope instability. Monitoring of pore-water pressure as an important part of the analysis is also needed.

References

[1] Sudjatmiko, *Geological Map of the Cianjur Quadrangle, Jawa Province, Scale 1:100000*, Indonesian Geological Research and Development Center, Bandung, Indonesia, 2003.

[2] Volcanology Survey Indonesia, Ministry of Energy and Mineral Resources, *Report on Soil Movement at Rongga Sub-District, West Bandung District, West Java Province*, site visit report, 2013. (Text in Indonesian).

[3] Volcanology Survey Indonesia, Ministry of Energy and Mineral Resources, *Report on Soil Movement at Saguling Sub-District, West Bandung District, West Java Province*, site visit report, 2014. (Text in Indonesian).

[4] Volcanology Survey Indonesia, Ministry of Energy and Mineral Resources, *Report on Soil Movement at Cipatat Sub-District, West Bandung District, West Java Province*, site visit report, 2014. (Text in Indonesian).

[5] Volcanology Survey Indonesia, Ministry of Energy and Mineral Resources, *Report on Soil Movement at Cipongkor Sub-District, West Bandung District, West Java Province*, site visit report, 2014. (Text in Indonesian).

[6] Volcanology Survey Indonesia, Ministry of Energy and Mineral Resources *Report on Soil Movement at Cipatat Sub-District, West Bandung District, West Java Province*, site visit report, 2015. (Text in Indonesian).
[7] Volcanology Survey Indonesia, Ministry of Energy and Mineral Resources, *Report on Soil Movement at Cipatat Sub-District, West Bandung District, West Java Province*, site visit report, 2016. (Text in Indonesian).
[8] Volcanology Survey Indonesia, Ministry of Energy and Mineral Resources, *Report on Soil Movement at Cipatat Sub-District, West Bandung District, West Java Province*, site visit report, 2018. (Text in Indonesian).
[9] Riyalda, B.F., Turyana, I., Santoso, E.W., *Web-based Landslide Disaster Information System Application (SI-Benar) Cililin district, West Bandung Regency* (in Indonesian), Jurnal Alami, **2**(2), pp. 131-138, Nov. 2018. DOI: 10.29122/alami.v2i2.
[10] LAPI ITB, *Slope Failure Remediation for Padang-Payakumbuh Access Road at Bottle Neck 1 Location, West Sumatera Province, Indonesia*, unpublished report, 2003. (Text in Indonesian).
[11] LAPI Ganeshatama, *Slope Failure Remediation for Sangatta-Perdau Access Road, East Borneo Province, Indonesia*, unpublished report, 2006. (Text in Indonesian).
[12] Kristo, C., Rahardjo, H. & Satyanaga, A., *Effect of Variations in Rainfall Intensity on Slope Stability in Singapore*, International Soil and Water Conservation Research, **5**(4), pp. 258-264, Dec. 2017. DOI: 10.1016/j. iswcr.2017.07.001.
[13] Rahardjo, H., Li, X.W. Toll, D.G. & Leong, E.C., *The Effect of Antecedent Rainfall on Slope Stability*, Journal of Geotechnical and Geological Engineering, Special Issue on Unsaturated and Collapsible Soils, **19**(3-4), pp. 371-399, Sep. 2001.DOI: 10.1007/978-94-015-9775-3_8
[14] Rahardjo, H., Leong, E.C. & Rezaur, R.B., *Effect of Antecedent Rainfall on Pore-water Pressure Distribution Characteristics in Residual Soil Slopes under Tropical Rainfall*, Hydrological Process, **22**(4), pp. 506-523, Feb. 2008. DOI: 10.1002/hyp.6880.
[15] Rahardjo, H., Ong, T.H. Ong, Rezaur, R.B., Leong, E.C. & Fredlund, D.G., *Response Parameters for Characterization of Infiltration*, Environmental Earth Sciences, **60**(7), pp. 1369-1380, Jun. 2010. DOI: 10.1007/s12665-009-0273-4.
[16] Rahardjo, H., Krisnanto, S. & Leong, E.C., *Effectiveness of Capillary Barrier and Vegetative Slope Covers in Maintaining Soil Suction*, Soils and Rocks, **39**(1), pp. 51-69, Jan. 2016. DOI: 10.28927/SR.391051.
[17] Gofar, N. & Lee M.L., *Extreme Rainfall Characteristics for Surface Slope Stability in the Malaysian Peninsular*, Georisk, **2**(2), pp. 65-78, Jun. 2008. DOI: 10.1080/17499510802072991.

[18] Li, W.C., Li, H.J., Dai, F.C. & Lee, M.L. *Discrete Element Modeling of a Rainfall-induced Flowslide*, Engineering Geology, **149**, pp. 22-34, Nov. 2012. DOI: 10.1016/j.enggeo.2012.08.006.

[19] Collins B.D. & Znidarcic, D., *Stability Analyses of Rainfall Induced Landslides*, Journal of Geotechnical and Geoenvironmental Engineering *ASCE*, **130**(4), pp. 362-372, Apr. 2004. DOI: (ASCE)1090-0241(2004) 130:4(362).

[20] Fredlund, D.G., Morgenstern, N.R. & Widger, R.A., *The Shear Strength of Unsaturated Soils*, Canadian Geotechnical Journal, **15**(3), pp. 313-321, Aug. 1978. DOI: 10.1139/t78-029.

[21] Fredlund, D.G., Rahardjo, H., *Soil Mechanics for Unsaturated Soils*, John Wiley & Sons, New York, 1993.

[22] Fredlund, D.G., Morgenstern, N.R., *Stress State Variables for Unsaturated Soils*, Journal of the Geotechnical Engineering Division, ASCE, **103**(GT5), pp. 447-466, May 1977. DOI: 10.1061/AJGEB6.0000423.

[23] Perera, Y.Y., Zapata, C.E., Houston, W.N. & Houston, S.L., *Prediction of the Soil-Water Characteristic Curve Based on Grain-Size-Distribution and Index Properties*, Geo-Frontiers Congress 2005, 2005. DOI: 10.1061/40776(155)4.

[24] Fredlund, D.G. & Xing, A., *Equations for the Soil-Water Characteristic Curve*, Canadian Geotechnical Journal, **31**(4), pp. 521-532, Aug. 1994. DOI: 10.1139/t94-061.

[25] Geocipta Bangun Optima, *Soil Investigation Report of Access Road at Cisokan, West Java Province, Indonesia*, Report No. GBO 07SI052019 CS PTPP, Jul. 2019. (Text in Indonesian).

[26] Geoslope International Ltd., *Seep/W User's Guide for Finite Element Analyses*, Calgary, Alberta, Canada, 2007.

[27] Bishop, A.W., *The Use of the Slip Circle in the Stability Analysis of Slopes*, Géotechnique, **5**(1), pp. 7-17, Mar. 1955. DOI: 10.1680/geot.1955.5.1.7

[28] Geoslope International Ltd., *Slope/W User's Guide for Finite Element Analyses*, Calgary, Alberta, Canada, 2007.

[29] Indonesian Ministry of Transportation, *Ministerial Regulation No. 60 on Technical Requirement of Railway*, 2012. (Text in Indonesian).

[30] Indonesian Ministry of Transportation, *Ministerial Regulation No. 81 on Safety Equipment for Road*, 2018. (Text in Indonesian).

[31] Chen F.W. & Liu C.W., *Estimation of the Spatial Rainfall Distribution using Inverse Distance Weighting (IDW) in the Middle of Taiwan*, Paddy and Water Environment, **10**(3), pp. 209-222, Sep. 2012. DOI: 10.1007/s10333-012-0319-1.

[32] ASTM D1586-18, *Standard Test Method for Penetration Test and Split-Barrel Sampling of Soils*, 2018.

[33] Terzaghi, K., Peck, R.B. & Mesri, G., *Soil Mechanics in Engineering practice*, ed. 3, John Wiley & Sons, New York, 1996.

[34] Holtz, R.D., Kovacs, W.D. & Seahan, T.C., *An Introduction to Geotechnical Engineering*, ed. 2, Pearson, Upper Saddle River, New Jersey, 2011.
[35] Skempton, A.W., *The Planning and Design of the New Hong Kong Airport, Discussion*, Proceedings Institute of Civil Engineers, London, **7**(2), pp. 305-307, 1957. DOI: 10.1680/ iicep.1957.2568.
[36] Carter, M. & Bentley, S.P., *Soil Properties and Their Correlations*, ed. 2, John Wiley & Sons, Chichester, West Sussex, 2016.
[37] Indonesian Bridge and Tunnel Road Safety Committee (KKJTJ), *Consensus of KKJTJ Jakarta in Year 2018*, unpublished report, 2018 (in Indonesian).
[38] Building Construction Advisory Committee Jakarta (TABG Jakarta), *Consensus of TABG Jakarta in Year 2016*, unpublished report, 2016. (Text in Indonesian).
[39] Sengara, I.W., *Suggested Effective Strength Parameters for Slope Stability Analysis for Jakarta-Bandung High Speed Railway Project*, Personal Communication, 2019.
[40] Shackelford, C.D. & Javed, F., *Large-Scale Laboratory Permeability Testing of a Compacted Clay Soil*, Geotechnical Testing Journal ASTM, **14**(2), 171-179, Jun. 1991. DOI: 10.1520/GTJ10559J.
[41] Lee, H.W. & Chang, P.W., *Correlation between the Laboratory and In-situ Permeabilities for the Embankments*, KSCE Journal of Civil Engineering, **11**(1), pp. 1-5, Jan. 2007. DOI: 10.1007/BF02823366.